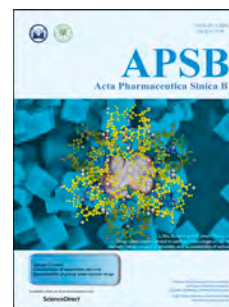


Journal Pre-proof

Self-assembling, pH-responsive nanoflowers for inhibiting PAD4 and neutrophil extracellular trap formation and improving the tumor immune microenvironment

Di Zhu, Yu Lu, Lin Gui, Wenjing Wang, Xi Hu, Su Chen, Yanming Wang, Yuji Wang



PII: S2211-3835(21)00439-1

DOI: <https://doi.org/10.1016/j.apsb.2021.11.006>

Reference: APSB 1262

To appear in: *Acta Pharmaceutica Sinica B*

Received Date: 9 July 2021

Revised Date: 13 September 2021

Accepted Date: 10 October 2021

Please cite this article as: Zhu D, Lu Y, Gui L, Wang W, Hu X, Chen S, Wang Y, Wang Y, Self-assembling, pH-responsive nanoflowers for inhibiting PAD4 and neutrophil extracellular trap formation and improving the tumor immune microenvironment, *Acta Pharmaceutica Sinica B*, <https://doi.org/10.1016/j.apsb.2021.11.006>.

This is a PDF file of an article that has undergone enhancements after acceptance, such as the addition of a cover page and metadata, and formatting for readability, but it is not yet the definitive version of record. This version will undergo additional copyediting, typesetting and review before it is published in its final form, but we are providing this version to give early visibility of the article. Please note that, during the production process, errors may be discovered which could affect the content, and all legal disclaimers that apply to the journal pertain.

© 2021 Chinese Pharmaceutical Association and Institute of Materia Medica, Chinese Academy of Medical Sciences. Production and hosting by Elsevier B.V. All rights reserved.

Original article

Self-assembling, pH-responsive nanoflowers for inhibiting PAD4 and neutrophil extracellular trap formation and improving the tumor immune microenvironment

Di Zhu^{a,b,†}, Yu Lu^{a,b,†}, Lin Gui^{a,b}, Wenjing Wang^c, Xi Hu^d, Su Chen^e, Yanming Wang^f, Yuji Wang^{a,b,*}

^a*Department of Medicinal Chemistry, College of Pharmaceutical Sciences of Capital Medical University, Beijing 100069, China*

^b*Beijing Area Major Laboratory of Peptide and Small Molecular Drugs, Engineering Research Center of Endogenous Prophylactic of Ministry of Education of China, Beijing Laboratory of Biomedical Materials, Beijing 100069, China*

^c*Beijing Institute of Hepatology, Beijing Youan Hospital, Capital Medical University, Beijing 100069, China.*

^d*Quantum Design China Ltd., Universal Business Park, Beijing 100015, China*

^e*Laboratory of Biomaterials and Biomechanics, Beijing Key Laboratory of Tooth Regeneration and Function Reconstruction, School of Stomatology, Capital Medical University, Beijing 100050, China*

^f*School of Life Sciences, Henan University, Kaifeng 475004, China*

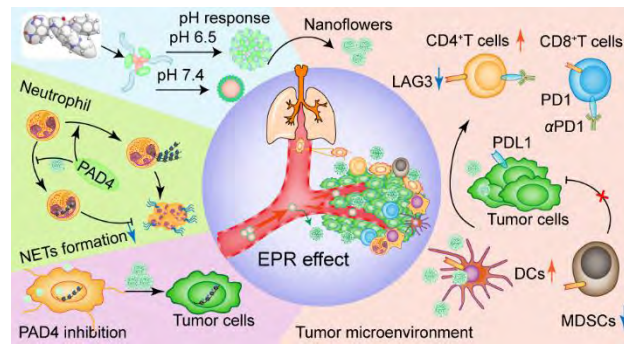
Received 9 July 2021; received in revised form 13 September 2021; accepted 10 October 2021

*Corresponding author. Tel./fax: +86 10 83911530.

E-mail address: wangyuji@ccmu.edu.cn (Yuji Wang).

[†]These authors made equal contributions to this work.

Running title: Nanoflowers inhibiting PAD4, NETs and regulating tumor immunity



ZD-E-1 targets tumors by binding PAD4 in response to pH and the enhanced permeability and retention (EPR) effect. It selectively inhibited tumor growth and metastasis by blocking NETs formation and improving the tumor immune microenvironment.

Abbreviations: CLSM, confocal laser scanning fluorescence microscopy; CSB, cell staining buffer; DCC, dicyclohexylcarbodiimide; DIPEA, *N,N*-diisopropylethylamine; DLS, dynamic light-scattering; DMF, *N,N*-dimethylformamide; FTMS, fourier-transform mass spectrometry; H3cit, histone 3 citrullination; HOBt, 1-hydroxybenzotriazole; IR, infrared spectroscopy; LAG3, lymphocyte activation gene-3; MS, mass spectrum; NETs, neutrophil extracellular traps; NMM, *N*-methylmorpholine; PAD4, peptidylarginine deiminase 4; PD1, programmed cell death 1; SEM, scanning electron microscope; TEM, transmission electron microscope; THF, tetrahydrofuran; UV, ultraviolet–visible spectroscopy.

Abstract Self-assembling carrier-free nanodrugs are attractive agents because they accumulate at tumor by an enhanced permeability and retention (EPR) effect without introduction of inactive substances, and some nanodrugs can alter the immune environment. We synthesized a peptidyl arginine deiminase 4 (PAD4) molecular inhibitor, ZD-E-1M. It could self-assembled into nanodrug ZD-E-1. Using confocal laser scanning microscopy, we observed its cellular colocalization, PAD4 activity and neutrophil extracellular traps (NETs) formation. The populations of immune cells and expression of immune-related proteins were determined by single-cell mass cytometry. ZD-E-1 formed nanoflowers in an acidic environment, whereas it formed nanospheres at pH 7.4. Accumulation of ZD-E-1 at tumor was pH-responsive because of its pH-dependent differences in the size and shape. It could enter the nucleus and bind to PAD4 to prolong the intracellular retention time. In mice, ZD-E-1 inhibited tumor growth and metastasis by inhibiting PAD4 activity and NETs formation. Besides, ZD-E-1 could regulate the ratio of immune cells in LLC tumor-bearing mice. Immunosuppressive proteins like LAG3 were suppressed, while IFN- γ and TNF- α as stimulators of tumor immune response were upregulated. Overall, ZD-E-1 is a self-assembling carrier-free nanodrug that responds to pH, inhibits PAD4 activity, blocks neutrophil extracellular traps formation, and improves the tumor immune microenvironment.

KEY WORDS pH-Response; Self-assembly; Carrier-free; Nanoflowers; Neutrophil extracellular traps; Single-cell mass cytometry; Tumor immune microenvironment; Lymphocyte activation gene-3

1. Introduction

Nano formulation of drugs is an effective strategy for cancer therapy because of its superior tumor targeting and aggregation properties¹⁻⁶. Drug release from many self-assembled nanocarriers can be controlled by pH and enzymes⁷⁻¹⁴. Investigators have used pH to trigger

morphological transformation of self-assembled nanoparticles into nanofibers⁷ and to modulate particle size for control of drug penetration and aggregation¹⁵. However, most nanocarriers present systematic toxicity¹⁶. Because these carriers themselves do not inhibit tumor growth but kill tumor cells by carrying other chemotherapy or radiation drugs¹⁷, the aggregation of these carriers may cause inflammation or toxicity. Thus, carrier-free nanodrugs are of great interest¹⁸ because they accumulate at tumor tissues by an enhanced permeability and retention (EPR) effect¹⁹ without introduction of inactive inert substances, and some self-assembled small molecules can alter the immune suppressive environment²⁰.

Peptidyl arginine deiminase 4 (PAD4) converts arginine to citrulline in histone 3^{21,22} and it has an important function in neutrophil extracellular traps (NETs) formation. PAD4 is overexpressed in many cancers, which is highly correlated with tumor growth and metastasis²³⁻²⁷. Thus, inhibition of PAD4 expression or activity and NETs formation are potential approaches for cancer therapy. In addition, PAD4 inhibitors block NETs formation by interfering with cytotoxic T cells and natural killer cell immune response^{24,28}.

Our purpose in this study was to synthesize self-assembling PAD4 inhibitors that had enhanced permeability and retention and could trigger the pH-responsive release of PAD4 inhibitors at the tumor site. The combination of active targeting achieved by PAD4 ligand–receptor interactions and passive targeting by the EPR effect and pH response was expected to achieve maximum inhibition. The pH of normal tissue is 7.4, whereas tumor tissues are mildly acidic with a pH of ~6.5^{15,29}. Thus, we designed a PAD4 inhibitor, ZD-E-1M, that contained a pH-responsive moiety nitrobenzoxadiazole^{30,31}. Like benzoxadiazole¹² and histidine^{13,31}, nitrobenzoxadiazole can be protonated at acidic pH. As a control to test the hypothesis that PAD4 inhibitors are effective antitumor agents, we synthesized ZD-BM that lacked the chloramidinium warhead (Fig. 1B).

We characterized the pH-responsive self-assembly of ZD-B and ZD-E-1 by transmission electron microscopy (TEM, Hitachi, JEM-2100, Tokyo, Japan) and scanning electron microscopy (SEM, Hitachi, S-4800, Tokyo, Japan), Fourier-transform mass spectrometry (FTMS, Bruker, SOLARIX-9.4T, Billerica, MA, USA) and NOSEY 2D NMR spectrum. We also observed nanostructure formation in cells at various pH using confocal laser scanning fluorescence microscopy (CLSM, Leica, TCS SP8 STED, Wetzlar, Germany) and fluorescence microscopy (Zeiss, Axio Observer.A1, Oberkochen, Germany). We used MTT assay to measure the cytotoxic effects of ZD-B and ZD-E-1 on various cancer and nontumor cell types. CLSM (Leica) and immunoblotting were used to measure the effect of ZD-E-1 on PAD4 activity and NETs formation; morphological changes were observed by TEM (Hitachi)

and SEM (Hitachi), and antimetastatic activity *in vitro* was measured with a Transwell assay. We assessed the antitumor and antimetastatic activities of the PAD4 inhibitor in S180 tumor-bearing mice and 4T1 orthotopic tumor-bearing mice. Lastly, we used single-cell mass cytometry (Fluidigm, Helios, San Francisco, CA, USA) to measure the population of immune cells and expression of immune-related proteins in LLC tumor tissues.

2. Materials and methods

2.1. Materials and reagents

Please refer to the Supporting Information for materials, reagents, and other methods.

2.2. Statistical analyses

Data are presented as mean \pm SD. Most statistical significance was evaluated by one-way ANOVA or *t*-test except that of tumor volume was evaluated by two-way ANOVA. Significance was set at $*P < 0.05$; extreme significance was set at $**P < 0.01$. Statistical analysis of cell and tissue section images was performed with ImageJ software (National Institutes of Health, Bethesda, MD, USA).

2.3. Preparation of nanodrugs ZD-B/ZD-E-1

The nanodrugs were prepared *via* the self-assembly method³²⁻³⁴. Briefly, the free drugs M/200 mg were dissolved in 50 μ L of dimethyl sulfoxide (DMSO) and diluted in 950 μ L of H₂O for 30 min under ultrasonic conditions. Another 4 mL of H₂O was added to prepare 1 mmol/L of nanodrugs for use as stock aqueous solutions. The solution pH was adjusted to 6.5 with 2 mol/L of HCl. Then, it was diluted to the desired concentration during the experiment.

2.4. Cellular localization and time-dependent drug uptake

The distribution of ZD-B and ZD-E-1 was observed with a laser confocal microscope (Leica, TCS SP8 STED, Wetzlar, Germany). The 4T1 cells were treated with 20 μ mol/L ZD-B and ZD-E-1 for 48 h. The nucleus was stained by DAPI. Images of distribution were captured at excitation 480 nm and emission 520 nm. Cells were incubated with drugs for 8, 16, 24 and 48 h.

2.5. NETs formation by neutrophils

C57BL/6 mice were sacrificed by cervical dislocation before the femurs were removed. The ends of bones were cut off to expose cavity and bone marrow suspension was collected with

PBS. Bone marrow single cell suspension was filtered through a 70 μm nylon screen. The neutrophils were isolated using the mouse neutrophil isolation kit (TBDSscience, LZS1100, Tianjin, China). Isolated neutrophils were administered immediately for 2 h after plating. Then NETs formation was induced for 2 h using 5 $\mu\text{mol/L}$ calcium ion carrier A23187 and the inhibitors, immediately. Finally, immunofluorescence staining of neutrophils was performed using H3cit antibody and observed by CLSM (Leica).

2.6. *In vivo antitumor and antimetastatic assay*

Male ICR mice, male C57BL/6 mice, and female BALB/C mice were purchased from Beijing Vital River Laboratory Animal Technology Co., Ltd. All animal experiments were executed according to the protocols approved by the Institutional Animal Care and Use Committee of Capital Medical University; the ethics number is AEEI-2018-174. The animals received humane care.

S180 cells were subcutaneously injected to form solid tumors. The subcutaneous tumors were implanted under mouse skin at the right armpit by injecting 0.2 mL of NS containing 4×10^6 cancer cells. When tumor size reached approximately 5 mm in diameter (4–5 days after implantation), the mice were divided randomly into different treatment groups with eight mice in each group. The tumor volume was measured every two days. The mice were administrated *via* tail vein (i.v.) for seven consecutive days. Twenty-four hours after the last administration, the mice were weighed and killed with ether anesthesia to obtain the organs and the tumor.

For 4T1 tumor studies, 5×10^5 tumor cells were subcutaneously injected around the third pair of breasts of 8-week-old BALB/c female mice. On Day 6, tumor size reached approximately 5 mm in diameter, and daily treatments with YW3-56 (10 $\mu\text{mol/kg}$) and ZD-E-1 (10, 5, and 2 $\mu\text{mol/kg}$) *via* i.v. injection were started. The mice were administrated every other day for 21 days.

For LLC tumor-bearing mice, LLC cells were subcutaneously injected to form solid tumors by injecting 0.2 mL of normal saline containing 3×10^6 tumor cells under the skin into the right armpit. When the tumor size reached approximately 5 mm in diameter (Day 5 after implantation), the mice were randomly divided into the following treatment groups: control: normal saline (i.v., 11 consecutive days, 10 mice), DOX (i.v. dose: 2 $\mu\text{mol/kg/day}$, 11 consecutive days, 10 mice), αPD1 (10 mg/kg, every 3 days, 10 mice), ZD-E-1 (10 $\mu\text{mol/kg/day}$, 11 consecutive days, 10 mice), and ZD-E-1 + αPD1 (10 mg/kg αPD1 and ZD-E-1, ZD-E-1 for 11 consecutive days and αPD1 every 3 days, 10 mice). Twenty-four hours after the last injection, the mice were weighed and killed with ether anesthesia, and the organs

and tumor were removed immediately. Mice in the survival curves experiment were treated as above.

3. Results and discussion

3.1. Chemistry

Supporting Information Scheme S1 shows the synthetic routes of the target compounds (see supporting file and paper³⁵ for complete details of synthesis). The peptides LV-OBzl and Orn(Boc)-NBzl (2E) were prepared according to the standard condensation reaction procedure. ZD-E-1M was obtained by converting the amino acid side chain to chloroacetamidine group. The structures and purities of ZD-BM and ZD-E-1M were confirmed by Fourier-transform mass spectra, Fourier-transform infrared spectroscopy, ¹H NMR, ¹³C NMR, HPLC, UV and fluorescence spectrum (Supporting Information Figs. S1–S25).

3.2. Design of self-assembling molecules

We described the PAD4 inhibitor YW3-56³⁵, which consisted of a naphthalene ring and an ornithine skeleton with chloramidine and benzylamine. We used YW3-56 as a lead compound to design and synthesize PAD4 inhibitors. ZD-BM and ZD-E-1M were screened by docking, scoring, and analyzing their interaction with PAD4^{36,37}. CDOCKER Energy in Supporting Information Table S1 shows that the interactions of ZD-BM and ZD-E-1M with PAD4 were both strong (48.755 and 47.628, respectively) and greater than that of YW3-56 (43.91). Fig. 1A and Supporting Information Fig. S26 showed the key amino acids and interaction forces between PAD4 and ZD-E-1M. Asp350 and Asp473 could stabilize chloroacetamidine group by hydrogen bonding and halogen, respectively, and properly position the imine carbon for nucleophilic attack. The departing amine was then protonated by His640. The carbonyl group could form a hydrogen bond with Arg374, which was specific to the peptidyl-arginine substrates compared to free arginine. The high potency of ZD-E-1M might be attributed to a hydrogen bond between benzoxadiazole and Trp347, and a π -alkyl with Arg639, which is unique to PAD4³⁸. To further illustrate the mechanism of compounds inhibiting PAD4, we determined the PAD4 inhibition activities as shown in Supporting Information Fig. S27A by a colorimetric method (Fig. S27B). Briefly, ZD-E-1M, ZD-BM and YW3-56 compete with the model substrate (BAEE) for the active site of PAD4. The IC₅₀ of ZD-E-1M inhibiting PAD4 was 2.390 μ mol/L, which was similar to that of YW3-56. This suggested that ZD-E-1M

inhibited PAD4 catalyzing histone citrullination by simulating the PAD4 substrate bound to the PAD4 active site (Fig. S27C).

Importantly, computer-aided drug design and PAD4 inhibition activities cannot guarantee that adequate concentration of drugs will be delivered to target cells; the delivered concentration is also related to the bioavailability of drugs, which is dependent on the shape and size of nanocarriers^{8,33,34,39}. Hence, we introduced the pH-responsive moiety nitrobenzoxadiazole (NBD) at the N-terminus of ornithine to confer pH-responsiveness (Fig. 1B). In addition, NBD served as a label because of its strong fluorescence in hydrophobic environments^{30,31}.

3.3. Characterization of the pH-responsive self-assembled nanodrugs

3.3.1. Shape and size of nanoparticles at different pH

The pH-responsive self-assembly properties of ZD-B and ZD-E-1 were assessed from three aspects. We observed the shape and size by TEM (Hitachi) and SEM (Hitachi) (Fig. 1C–F). The average hydrodynamic diameters were measured by dynamic light-scattering (DLS, Brookhaven, Nano-ZS90, Holtsville, NY, USA), and the zeta potential was determined for six days (Fig. 1G). At pH 7.4, TEM and SEM images showed that ZD-B had a dendritic crystal structure with length over 1000 nm, width 100–300 nm, and nanospheres with size 60–240 nm (Fig. 1C). ZD-E-1 was spherical with diameters from 30 to 100 nm (Fig. 1E). At pH 6.5, TEM and SEM images showed that ZD-B and ZD-E-1 self-assembled into a flower-like and loose nanostructure, 400 and 200 nm, respectively (Fig. 1D and F). The sizes of the nanodrugs increased in the acidic condition. This increase may have resulted from a looser structure induced by the acidic microenvironment^{13,14,40,41}.

The size distribution (Supporting Information Fig. S28A–D) of ZD-B and ZD-E-1 at pH 7.4 and 6.5 in TEM photos were similar to the diameter measured by light scattering in solution (Fig. 1G). The size of ZD-B remained ~300 nm stably in water and did not change with decreasing pH for six days. As the pH decreased, the size of ZD-E-1 increased notably, from 80 nm (pH 7.4) to 208 nm (pH 6.5). With increasing time, the sizes of ZD-B and ZD-E-1 were stable in solution at pH 6.5 and 7.4. In addition, the zeta potentials of ZD-B and ZD-E-1 were stable in solution at pH 6.5 and 7.4, from –5 to –15 mV (Fig. 1H). The negative zeta potential was likely the result of the strongly electron-withdrawing nitro group. As the pH decreased, the zeta potential of ZD-B changed slightly, whereas the zeta potential of ZD-E-1 decreased, from –15 to –10 mV. This decreased zeta potential indicated that the nitrobenzoxadiazole group was protonated to form a hydrophilic chain from a hydrophobic

chain^{7,42}. Besides, we also found that the particle size and zeta potential of ZD-E-1 remain stable when the concentration is greater than 0.001 mg/mL concentration (Fig. S28E and S28F).

3.3.2. Critical aggregation concentration (CAC) and drug release of nanodrugs at different pH

To characterize the self-assembly properties of nanoparticles, the critical aggregation concentration (CAC)⁴³ and drug release curve⁴⁴ at different pH values (Figs. 1J–K and Supporting Information Fig. S29) were determined. At pH 7.4, the CAC of ZD-B was similar to that of ZD-E-1, about 15 $\mu\text{mol/L}$. With the decrease of pH value, CAC values of ZD-B and ZD-E-1 were increased to 30 and 50 $\mu\text{mol/L}$, respectively. This suggested that the nanoflowers structure made it easier for nanodrugs to release. As shown in Fig. S29C, there was almost no release of ZD-B at pH 7.4 and 6.5, whereas ZD-E-1 could be released over time. The accumulative drug release rate of ZD-E-1 at pH 6.5 reached 99.0% at 8 h, while it reached about 90% at pH 7.4. This illustrated that the nanoflower structure was contributed to drug release rate at tumor site.

3.4. Principles of the self-assembled molecules

We used Fourier-transform mass spectra, NOSEY 2D NMR spectroscopy, and material studio (BIOVIA, San Diego, CA, USA) to identify molecules in solution^{45,46}. Fig. 2A and B show the FTMS spectra of ZD-B and ZD-E-1 in ultrapure water. There was an existence of dimeric (967.4319 and 919.3070) and trimeric (1450.6859 and 1378.4527) supermolecules in ZD-B and ZD-E-1 spectra, respectively, and even the tetramer (1933.9432) and pentamer (2418.1988) were detected in ZD-B spectrum⁴⁷. These larger forms indicated that several small molecules first aggregated into self-assembled units in solution. The FTMS spectra of ZD-B and ZD-E-1 at pH 6.5 (Supporting Information Fig. S30A and S30B) show the nanodrug self-assembly units are similar to that in neutral environment.

To investigate the interaction pattern, we recorded NOESY spectra of ZD-B and ZD-E-1 at pH 6.5 and 7.4 in deuterated solvent. Fig. 2C shows one interesting cross-peak of ZD-B resulted from the interaction of H near the nitro of the NBD residue of one molecule with the chiral carbon H of the valine residue of another molecule. This interaction indicated that the distance between the NBD residue and benzylamine residue was less than 4 Å. Fig. 2D shows four cross-peaks of ZD-E-1. Cross-peaks 1 and 4 resulted from the interaction of H near the nitro of the NBD residue of one molecule with the benzene ring H and methylene H of

benzylamine of another molecule, respectively. Cross-peaks 2 and 3 resulted from the interaction of H away from nitro of the NBD residue of one molecule with the chloromethyl H of amino acid side chain and benzene ring H of benzylamine of another molecule, respectively. This interaction suggested that the distances between the NBD residue of one molecule and the benzylamine residue or side chain of another molecule were both less than 4 Å. The NOSEY 2D NMR spectrum in pH 6.5 deuterated solvent was similar to the spectrum at pH 7.4 (Fig. S30C and S30D). The main difference was that cross-peak 1 became deeper and cross-peak 3 became lighter in acidic environments, which indicated that the intermolecular interaction angle of protonation was adjusted slightly.

By combining the results of FTMS spectra and NOSEY 2D NMR, we clarified the interaction of the self-assembled unit. First, FTMS spectra confirmed that there were five molecules of ZD-BM and three molecules of ZD-E-1M in the self-assembled units, respectively. Second, cross-peaks in NOSEY spectrum identified the spatial position of groups. Finally, five molecules of ZD-BM or three molecules of ZD-E-1M were packed together in Discovery Studio (Neotrident, Beijing, China) to give the conformation of self-assembled units (Fig. 2E and F).

We also used a Material Studio molecular dynamics (MD) simulation technique to examine self-assembly of the nanodrugs in normal and acidic pH. The MD simulation of ZD-BM showed that 1200 molecules could form a spherical structure of diameter ~118 nm at pH 7.4 (Fig. 2E) and a multi-space spherical structure of diameter ~128 nm at pH 6.5 (Fig. S30E). The MD simulation of ZD-E-1M (Fig. 2F) showed that 900 molecules formed a nanosphere of diameter ~96 nm in normal pH, while that of ZD-E-1M with H⁺ (Fig. S30F) showed a looser structure of diameter ~118 nm. The simulated particle size was related to the number of molecules in the box. Therefore, the simulated particle size is not exactly equal to the actual particle size. The simulated particle size is equal to or a fraction of the actual particle size.

3.5. Intracellular morphology and localization of self-assembled molecules

To study the pH-responsive transformation of ZD-B and ZD-E-1 on the cell surface and inside the cell, we incubated normal HL7702 cells and 4T1 tumor cells with the nanoparticles for 48 h. Intracellular morphology and localization of the nanoparticles were observed by fluorescence and CLSM (Leica). Fluorescence microscope images (Fig. 3A) showed dendritic fluorescent structures self-assembled on the surface of HL7702 cells treated with 50 µmol/L ZD-B. This dendritic appearance was similar to the shape in solution at pH 7.4 (Fig. 1C). To observe the nanodrug inside the cells, we acquired CLSM images of HL7702 cells treated

with 20 $\mu\text{mol/L}$ ZD-B (Fig. 3A). Only a few fluorescent spots were observed and dendritic fluorescence signal was not determined, which indicated that the dendritic structures did not enter the normal cells. Similarly, HL7702 cells treated with 20 $\mu\text{mol/L}$ ZD-E-1 (Fig. 3B) showed only a few fluorescent spots in the cytoplasm and no fluorescence in the nucleus. This result suggested that only a small amount of ZD-E-1 entered the normal cell cytoplasm.

Fig. 3C shows that, in 4T1 tumor cells, ZD-B was distributed in the cytoplasm, and some nano-level strong fluorescent spots were observed. Thus, ZD-B was transformed into nanoparticles in the acidic tumor environment. Fig. 3D shows that ZD-E-1 was widely distributed throughout the cells, and strong fluorescence was observed as dot-like structures in the nucleus. These observations coincided with the self-assembly behavior of ZD-B and ZD-E-1 in acid solution. However, the sizes of the structures were too small in CLSM images to ascertain whether the fluorescent nanodots were flower-like. Fig. 3E shows the statistical diagrams of mean fluorescence intensities of 4T1 tumor cells and normal cells treated with ZD-B and ZD-E-1. Both drugs showed very low uptake in normal cells, but uptake was greater in tumor cells. This may be because the endocytosis rate in tumor cells is faster than that of normal cells⁴⁸. And the tumor cells expressed a relatively high PAD4 protein amount, which resulted in the significantly enhanced cellular uptake of ZD-E-1²⁴.

3.6. Cytotoxicity

We measured cytotoxic effects of ZD-B and ZD-E-1 on different tumor cell lines and normal cells (Supporting Information Table S2). ZD-B and ZD-E-1 had the lowest cytotoxicity towards the normal HL7702 cells. As shown in Fig. 3F, only 100 $\mu\text{mol/L}$ ZD-E-1 could decrease the viability of HL7702 cells to below 50%. Under the same condition, ZD-B and ZD-E-1 had a greater cytotoxic effect on tumor cells compared with normal cells. ZD-E-1 exhibited the greatest inhibitory activity against the 4T1 cell line (which expressed a relatively high PAD4 protein amount²⁴), and the IC_{50} (~ 8 $\mu\text{mol/L}$) was 3–6 times lower than that of other cancer cell lines. Treatment with 100 $\mu\text{mol/L}$ ZD-B and ZD-E-1 both decreased 4T1 cell growth (Fig. 3G). However, the IC_{50} of ZD-E-1 was 7.93 $\mu\text{mol/L}$, whereas that of ZD-B was 94.79 $\mu\text{mol/L}$ (Fig. 3H). This difference in IC_{50} value coincided with the difference in drug uptake (Fig. 3E). The cytotoxicity of nanodrugs increased with their increasing cellular uptake⁴⁹.

3.7. Time-dependent change in cell uptake

To assess time-dependent drug uptake, we observed drug distribution by CLSM (Leica) and counted the average fluorescence intensity in cells at each time point. Fig. 3I and J show that ZD-B was rapidly distributed in the cytoplasm at 8 h, and the fluorescence intensity decreased gradually with time. We observed many fluorescent spots in the cytoplasm at 16 h. However, many fluorescent spots were seen spreading out of the cytoplasm at 24 h. By 48 h, only a small number of fluorescent points remained in the cytoplasm. ZD-E-1 accumulated in cells gradually with time until 48 h, when cells were presumed floating and dead. This difference may have occurred because ZD-B was too large to enter the nucleus to bind PAD4 and it was excreted from the cells⁵⁰.

3.8. Uptake behavior and uptake pathway

To determine the uptake behavior, we measured the uptake of ZD-E-1 and ZD-B in different pH on the normal cells and tumor cells by HPLC-MS (SCIEX, Triple Quad 6500+, Framingham, MA, USA) and flow cytometry (BD, LSRFortessa SORP, Franklin Lakes, NJ, USA). As shown in Supporting Information Fig. S31A, the results of HPLC-MS showed that the uptake amount of ZD-E-1 in 4T1 cells was higher than that in HL7702 cells at pH 7.4 and 6.5 at 48 h. This was consistent with the results of CLSM in Fig. 3E. At the same time, the results of flow cytometry in Fig. S31B showed that the uptake amount of ZD-E-1 was higher than that of ZD-B in 4T1 cells at pH 7.4 and 6.5 at 48 h. This may be due to the different size of ZD-B and ZD-E-1. The nanoparticles with size less than 300 nm are more likely to enter the cells readily by endocytosis^{51,52}. And the drug release rate of ZD-B was much lower than that of ZD-E-1. Besides, the uptake of ZD-B and ZD-E-1 at pH 6.5 were significantly higher than that at pH 7.4. It suggested that the nanoflower structure was more conducive to cellular uptake.

The uptake pathway was assessed by the addition of different endocytosis inhibitors. Chlorpromazine (CPZ), methyl- β -cyclodextrin (M- β -CD), and amiloride hydrochloride (AM) inhibit clathrin-dependent endocytosis, caveolae-mediated endocytosis, and micropinocytosis, respectively. As shown in Fig. S31C, the fluorescence intensity did not decrease after the endocytosis inhibitors were added. In contrast, the fluorescence intensity increased with the addition of CPZ and M- β -CD. This result suggested that clathrin- and caveolae-mediated endocytosis may be “weak links”⁵³.

3.9. H3cit protein expression in 4T1 cells

To clarify the mechanism of PAD4 inhibition by the compounds in 4T1 cells, we used CLSM (Leica) and immunoblotting to measure histone H3 citrullination (H3cit). In Fig. 4A and Supporting Information Fig. S32A, the blue, red, and green represent nucleus, H3cit, and drugs, respectively. ZD-E-1 was concentrated mainly in the nucleus and the area near the nucleus. Strong dot-like fluorescence was observed in the nucleus. At the site where the drug (green) fluorescence was concentrated, the H3cit (red) fluorescence diminished (Fig. 4B). This change in fluorescence suggested that the citrullination of histones was reduced at the site where the nanoparticles were concentrated. In addition, Fig. 4C shows the mean fluorescence intensity of H3cit proteins with various treatments. Both ZD-E-1 and YW3-56 reduced the expression of H3cit and there was no significant difference in the H3cit protein expression between the two groups. The results in Immunoblotting (Fig. S32B and C) were coincident with that observed by CLSM (Leica).

3.10. Effect of drugs on NETs formation by neutrophils

To observe the effect of the drugs on NETs release from neutrophils, we stimulated neutrophils from femoral bone of C57BL/6 with 5 $\mu\text{mol/L}$ A23187 for 2 h to release NETs. Fig. 4D shows the release of extracellular chromatin and H3cit from neutrophils in the control and ZD-B groups. NETs formation decreased after administration of YW3-56 and ZD-E-1, and the intracellular H3cit fluorescence was also darkened. Thus, ZD-E-1 reduced NETs formation and there was no significant difference with the YW3-56 group (Fig. 4E). Interestingly, neutrophils still engulfed larger amounts of nanodrugs at normal pH, probably because neutrophils are highly phagocytic⁵⁴.

3.11. Antimigration of 4T1 cells

To examine the antimetastatic ability of ZD-E-1 *in vitro*, we conducted Transwell assays. Fig. 4F and G show that the number of 4T1 cells passing through the Transwell membrane pores decreased significantly after ZD-E-1 treatment, and tumor metastases were inhibited in a dose-dependent manner. There was no significant difference in the inhibition effect between the high doses (10 and 5 $\mu\text{mol/L}$) and the positive group tetrapeptide RGDS.

3.12. Cell morphology by TEM and SEM

We used TEM (Hitachi) to examine the entire and local features of 4T1 cells treated with ZD-E-1 and PBS. The size of tumor cells treated with ZD-E-1 was smaller compared with the untreated 4T1 cells (Fig. 4H). In treated cells, the number of mitochondria increased, and the

mitochondria had swelled obviously. The nuclei of cells treated with ZD-E-1 shrank, and the morphology was irregular. Besides, we performed SEM (Hitachi) to determine the morphological changes of cell surfaces in treated and untreated cells. Fig. 4I showed that ZD-E-1-treated cells became smaller compared with the untreated cells, which agreed with the TEM morphological analysis. The cells became rounder after ZD-E-1 treatment. The number of pseudopodia decreased, and the length shortened. With increasing nanodrug dose, the cell junctions became loose, and the intercellular spaces were enlarged. The results suggested that ZD-E-1 inhibited tumor cell metastasis⁵⁵.

3.13. Antitumor effect of ZD-B and ZD-E-1 in S180 tumor-bearing mice

To evaluate antitumor activity *in vivo*, the nanodrugs were administered by tail vein injection of S180 tumor-bearing mice. After seven days, the tumor volume and weight (Fig. 5A and B) suggested that ZD-E-1 suppressed tumor growth in a dose-dependent manner. ZD-E-1 inhibited tumor growth significantly at 5 $\mu\text{mol/kg}$, whereas the same dose of ZD-B did not produce a significant difference compared with the control group.

3.14. Distribution of ZD-B and ZD-E-1 *in vivo*

3.14.1. Immunofluorescence analysis on cryosections

To locate ZD-B and ZD-E-1 in tumor tissue, we prepared frozen sections. After administration, ZD-E-1 decreased the mean fluorescence intensity of H3cit effectively (Fig. 5C). The images in Fig. 5D show that the ZD-E-1 nanodrug aggregated in the tumor tissue, and green fluorescence of ZD-E-1 was observed in the nucleus and cytoplasm of tumor cells, whereas no green fluorescence was observed in tumor tissues treated with ZD-B. Thus, the nanodrug ZD-E-1 possessed greater permeation in the tumor tissues. In addition, at the site where the green fluorescence was concentrated, the red fluorescence of H3cit weakened (Fig. 5E). This situation agreed with CLSM results from cells *in vitro*. The fluorescence changes supported the conclusion that ZD-E-1 inhibited citrullination of H3 catalyzed by PAD4.

3.14.2. Fluorescence imaging

To determine the distribution of nanodrug *in vivo*, three S180 tumor-bearing ICR mice per time point were sacrificed at 0.5, 2, 8 and 24 h after single dose administration and then imaged and analyzed for radiant efficiency (Fig. 5F and G). At 0.5 h, green fluorescence of ZD-E-1 was widely distributed in tumor and organs, especially liver and kidney. Accumulation in liver and kidney in the early phase occurred probably because those organs

are the main metabolic tissues. The signal in kidney and tumor in the ZD-E-1 treated group persisted up to 8 h, whereas the fluorescence of the ZD-B group disappeared by 2 h. Thus, the ZD-E-1 nanodrug possessed longer retention in the tumor tissues.

3.15. $CD4^+/CD8a^+$ cells in tumor tissues

CD4 and CD8 are specific proteins in tumor-infiltrating lymphocytes, and the occurrence of tumor-specific CD4 and CD8 T cells in tumor tissue is regarded as a favorable prognostic factor⁵⁵. Immunohistochemical methods were used to measure the number of $CD4^+$ and $CD8a^+$ T cells in tumor tissues (Fig. 5H and I). The number of CD4 and CD8a increased significantly in the 10 $\mu\text{mol/kg}$ group; thus, ZD-E-1 increased the tumor infiltration of CD4 and CD8 T cells. This may be related to the effect on NETs formation²⁴ and tumor immune microenvironment⁵⁶. Thus, we designed the next experiments.

3.16. Antitumor and antimetastatic effect of ZD-E-1 in 4T1 orthotopic tumor-bearing mice

To further confirm the activities and molecular mechanism of ZD-E-1 *in vivo*, we measured antitumor and antimetastatic effects in 4T1 orthotopic tumor-bearing mice. Fig. 6A–C show volume and tumor weight. Compared with the vehicle group, the tumor weight of the 4T1 mice that received 10 and 5 $\mu\text{mol/kg}$ ZD-E-1 was decreased, which indicated that ZD-E-1 inhibited the growth of primary tumor in a dose-dependent manner. Compared with the YW3-56 group (10 $\mu\text{mol/kg}$, i.v.), there was no difference in tumor weight for either the same dose of ZD-E-1 (10 $\mu\text{mol/kg}$) or the lower dose (5 $\mu\text{mol/kg}$). From the curve of tumor volume change, the tumor volume of treatment groups decreased from Day 11. All dose groups presented differences compared with the vehicle group on Day 21 (see Fig. 6A).

To assess the ability of the 4T1 tumors to metastasize, we counted the number of nodules in lungs and quantitated metastatic foci after Hematoxylin–Eosin (H&E) staining. Fig. 6D and E show that 10 and 5 $\mu\text{mol/kg}$ ZD-E-1 decreased the number of macroscopic pulmonary metastases. The antimetastatic activities of these groups were better than or equal to that of the YW3-56 group. H&E staining of lung tissues (Fig. 6F) showed that ZD-E-1 reduced the number of lung metastases. In addition, the H&E results showed that the inflammatory cell infiltration into the lungs was still present in the ZD-E-1 and YW3-56 treatment groups.

3.17. Effect of ZD-E-1 on ability of neutrophils in tumor tissues to release NETs

To assess the effect of ZD-E-1 on NETs formation, we marked neutrophils with Ly6G and observed the expression of H3cit in neutrophil-enriched regions to represent the density of

NETs. Fig. 6G and H show that the H3cit expression in neutrophil-enriched areas decreased after YW3-56 and ZD-E-1 treatment. It suggested that YW3-56 and ZD-E-1 blocked NETs formation in tumor tissues, thus preventing tumor growth and metastasis.

3.18. Nanotoxicity of ZD-E-1

To assess nanodrug toxicity, we performed a histological analysis by H&E staining. The H&E sections (Supporting Information Fig. S33A) showed that there was no noticeable damage in major organs such as heart, liver, spleen, and kidney treated with ZD-E-1 while the liver cells in the YW3-56 group were sparse and arranged in disorder with the nucleus pyknotic. Considering that liver and kidney may be the target organs for drug accumulation, we measured the concentrations of ALT, AST, creatinine (Crea), and urea (Fig. S33B–S33E). There were no significant changes in serum concentrations of any of those components. Thus, we concluded that the nanodrug ZD-E-1 did not cause systemic toxicity.

3.19. Effect of ZD-E-1 on tumor immune microenvironment

To study the effects of ZD-E-1 on the immune microenvironment in tumor tissues, we dispersed tumor tissues into cell suspensions for single-cell mass cytometry analysis (Fig. 7A)⁵⁷. Supporting Information Fig. S34 and Table S3 show the gating hierarchy plots for tumor immune analysis and penal of mass cytometry. The proportions of various immune cells (Fig. 7C) were measured by analyzing the expression of cell surface markers (Fig. 7A). The proportion of dendritic cells (DCs) and CD4 T cells in tumor tissues increased significantly, whereas the proportion of myeloid-derived suppressor cells (MDSCs) decreased (Fig. 7D). DCs are antigen-presenting immune cells that promote activation of T cells⁵⁸. MDSCs are early myeloid progenitors of granulocytes, macrophages, and DCs that mediate immune suppression⁵⁹. The changes in proportion of immune cells indicated that ZD-E-1 ameliorated the tumor immune microenvironment. In addition, the expression of lymphocyte-activation gene-3 (LAG3) protein in different immune cells was generally reduced (Fig. 7E). Inhibitory receptor LAG3 is a potential cancer immunotherapeutic target on the T-cell surface, despite PD-1 and CTLA4 immune checkpoints⁶⁰. Many investigators suggested that inhibition of LAG3 and PD-1 enhances antitumor immunity⁶¹. Combination with PD1 antibody (α PD1) and ZD-E-1 may lead to better antitumor effects. Expression of CXC chemokine receptor 3 (CXCR3) for CD4 T cells and CC chemokine receptor 4 (CCR4) for CD8 T cells increased significantly (Fig. 7F). This increase may stimulate T cell activation and infiltration. In sum,

ZD-E-1 ameliorated the tumor immune microenvironment by regulating the ratio of immune suppressive cells to immune active cells and immune related proteins (Fig. 7G).

3.20. Combination immunotherapy with PAD4 inhibitor and PD1 antibody on LLC tumor-bearing mice

To further investigate combination immunotherapeutic activities with PAD4 inhibitor ZD-E-1 and PD1 antibody (α PD1), C57BL/6 mice bearing LLC tumor were treated with different drugs (Fig. 8A). The tumor volume and tumor weight showed that ZD-E-1 or α PD1 alone could prevent primary tumor growth (Fig. 8B–D). Combined treatment with ZD-E-1 and α PD1-decreased tumor growth significantly compared with that treated with α PD1 or ZD-E-1 alone. After combination therapy, the tumor inhibition rate was raised from 34.2% (ZD-E-1 treatment) and 37.7% (α PD1 treatment) to 58.2% (combined treatment). In addition, combined treatment with ZD-E-1 and α PD1 has similar inhibition activity in tumor metastasis as the RGDS treatment group, ZD-E-1 or α PD1 alone treatment group (Figs. 8E–G). Combined treatment group also prolonged the survival time of LLC tumor-bearing mice than ZD-E-1 or α PD1 alone treatment group significantly (Fig. 8H). Moreover, despite the DOX group showed similar tumor suppressive properties with combined treatment group, it could not inhibit lung metastasis. Besides, the mice body weight (Supporting Information Fig. S35A) and main organs weight (Fig. S35B–F) in the DOX group were decreased significantly compared with NS and other groups. ALT, AST, urea and Crea levels of combined treatment group has no significant change with that in NS group (Fig. S35G–S35J). This indicated that combined treatment showed no systematic toxicity.

3.21. Effect of combination immunotherapy on tumor immune environment and inflammatory factors

To validate the findings of single-cell mass cytometry analysis, tumor tissue sections were stained by immunofluorescence for LAG3. The represented pictures and statistical analysis in Fig. 8I and J showed that the mean fluorescence of LAG3 in the ZD-E-1 and combined treatment group decreased significantly. The results were consistent with that of mass cytometry. This suggested that ZD-E-1 indeed reduced the level of LAG3 to improve tumor immune environment. Moreover, the cytokines IFN- γ and TNF- α as stimulators of the tumor immune response were upregulated in tumor tissues and serum (Fig. 8K and L). This may be the reason why ZD-E-1 increased the infiltration of CD4 cells and DCs while decreased the aggregation of MDSCs.

3.22. The serum stability and pharmacokinetics

The serum stability and pharmacokinetics of ZD-E-1 were determined by HPLC–MS (SCIEX)^{44,62}. As shown in Supporting Information Fig. S36A, the half-life of ZD-E-1 in serum *in vitro* was 5.79 h. This indicated that the cycle time of ZD-E-1 was much longer than that of YW3-56 (5 min)⁶³. Besides, nanodrug ZD-E-1 remains in circulation for more than 48 h and there was a fast release within the first half an hour (Fig. S36B). This provided a sustained release of the molecules.

4. Discussion and conclusion

We created a novel carrier-free nanodrug ZD-E-1. As shown in Fig. 9, the drug acts by the EPR effect, responding to pH, and inhibiting PAD4. The combination of active PAD4 inhibition and passive pH and EPR improved tumor targetability and enhanced permeability. The nanodrug ZD-E-1 exhibited in a flower-like nanostructure in acidic solution, and this structure was looser than the structure at pH 7.4. The nanoflower structure was favored for long-term accumulation of the nanodrug at the tumor site, for selective delivery of the drugs into tumor cells, and for subsequent cytotoxicity.

In addition, the drug inhibited tumor growth and metastases by inhibiting histone 3 citrullination and blocking NETs formation *in vivo* and *in vitro*. We also did not find changes of ALT, AST, creatinine, or urea concentrations in serum, although nanodrug ZD-E-1 may be eliminated by renal excretion and hepatic metabolism. The absence of change in serum components indicated that ZD-E-1 was not toxic to the mouse liver or kidney. Furthermore, a combination of ZD-E-1 and PD-1 antibody produced an enhanced antitumor and antimetastatic effect on LLC tumor-bearing mice, and prolonged survival. On the one hand, one study²⁴ has found that inhibition of NETs sensitizes tumors to PD-1 and CTLA-4 checkpoint blockade. Thus, ZD-E-1 could increase the anti-tumor effects of α PD-1 by blocking the NETs formation. On the other hand, ZD-E-1 could inhibit the expression of LAG3 protein. Inhibition of LAG3 and PD-1 enhances antitumor immunity. Thus, this may be another cause that ZD-E-1 could increase the anti-tumor effects of α PD-1.

Although PAD4 inhibitors can kill cancer cells selectively and reprogram the immunosuppressive microenvironment, the mechanism of ZD-E-1 immune reprogramming is unknown. The STAT3 pathway may be involved in tumor immunomodulation^{64,65} and PAD4 may be related to this pathway.

Acknowledgements

This work was supported by the Beijing Municipal Colleges and Universities High Level Talents Introduction and Cultivate Project—Beijing Great Wall Scholar Program (CIT&TCD 20180332, China).

Author contributions

Di Zhu, Yu Lu and Yuji Wang designed the research. Di Zhu and Yu Lu carried out the experiments and performed data analysis. Lin Gui, Xi Hu, Wenjing Wang and Xi Hu participated part of the experiments. Yanming Wang and Yuji Wang provided experimental drugs and quality control. Di Zhu and Yu Lu wrote the manuscript. Yuji Wang and Su Chen revised the manuscript. All of the authors have read and approved the final manuscript.

Conflicts of interest

The authors have no conflicts of interest to declare.

References

1. Devadasu VR, Bhardwaj V, Kumar MNVR. Can controversial nanotechnology promise drug delivery?. *Chem Rev* 2013;**113**:1686-1735.
2. Madamsetty VS, Pal K, Dutta SK, Wang E, Mukhopadhyay D. Targeted dual intervention-oriented drug-encapsulated (DIODE) nanoformulations for improved treatment of pancreatic cancer. *Cancers* 2020;**12**:1189.
3. Wang BJ, Zhang W, Zhou XD, Liu MN, Hou XY, Cheng ZT, et al. Development of dual-targeted nano-dandelion based on an oligomeric hyaluronic acid polymer targeting tumor-associated macrophages for combination therapy of non-small cell lung cancer. *Drug Deliv* 2019;**26**:1265-79.
4. Chaturvedi VK, Singh A, Singh VK, Singh MP. Cancer nanotechnology: a new revolution for cancer diagnosis and therapy. *Curr Drug Metab* 2019;**20**:416-29.
5. Alavi M, Hamidi M. Passive and active targeting in cancer therapy by liposomes and lipid nanoparticles. *Drug Metab Pers Ther* 2019;**34**:20180032.
6. Arranja AG, Pathak V, Lammers T, Shi Y. Tumor-targeted nanomedicines for cancer theranostics. *Pharmacol Res* 2017;**115**:87-95.
7. Yang PP, Luo Q, Qi GB, Gao YJ, Li BN, Zhang JP, et al. Host materials transformable in tumor microenvironment for homing theranostics. *Adv Mater* 2017;**29**:1605869.

8. Hu XX, He PP, Qi GB, Gao YJ, Lin YX, Yang C, et al. Transformable nanomaterials as an artificial extracellular matrix for inhibiting tumor invasion and metastasis. *ACS Nano* 2017;**11**:4086-96.
9. Xu ZX, Zhuang XD, Yang CQ, Cao J, Yao ZQ, Tang YP, et al. Nitrogen-doped porous carbon superstructures derived from hierarchical assembly of polyimide nanosheets. *Adv Mater* 2016;**28**:1981-7.
10. Liu YC, Wang B, Ji XH, He ZK. Self-assembled protein-enzyme nanoflower-based fluorescent sensing for protein biomarker. *Anal Bioanal Chem* 2018;**410**:7591-8.
11. Zhang P, Wang F, Wang Y, Li S, Wen S. Self-assembling behavior of pH-responsive peptide A6K without end-capping. *Molecules* 2020;**25**:2017.
12. Liao RQ, Lv P, Wang Q, Zheng JN, Feng B, Yang B. Cyclodextrin-based biological stimuli-responsive carriers for smart and precision medicine. *Biomater Sci* 2017;**5**:1736-45.
13. Lee ES, Oh KT, Kim D, Youn YS, Bae YH. Tumor pH-responsive flower-like micelles of poly(L-lactic acid)-*b*-poly(ethylene glycol)-*b*-poly(L-histidine). *J Control Release* 2007;**123**:19-26.
14. Hwang JH, Choi CW, Kim HW, Kim DH, Kwak TW, Lee HM, et al. Dextran-*b*-poly(L-histidine) copolymer nanoparticles for pH-responsive drug delivery to tumor cells. *Int J Nanomedicine* 2013;**8**:3197-207.
15. Wu W, Luo L, Wang Y, Wu Q, Dai HB, Li JS, et al. Endogenous pH-responsive nanoparticles with programmable size changes for targeted tumor therapy and imaging applications. *Theranostics* 2018;**8**:3038-58.
16. Poon W, Zhang YN, Ouyang B, Kingston BR, Wu JLY, Wilhelm S, et al. Elimination pathways of nanoparticles. *ACS Nano* 2019;**13**:5785-98.
17. Bertrand N, Wu J, Xu XY, Kamaly N, Farokhzad OC. Cancer nanotechnology: the impact of passive and active targeting in the era of modern cancer biology. *Adv Drug Deliver Rev* 2014;**66**:2-25.
18. Yang MY, Zhao RR, Fang YF, Jiang JL, Yuan XT, Shao JW. Carrier-free nanodrug: a novel strategy of cancer diagnosis and synergistic therapy. *Int J Pharm* 2019;**30**:570:118663.
19. Wang ZR, Chen JW, Little N, Lu JQ. Self-assembling prodrug nanotherapeutics for synergistic tumor targeted drug delivery. *Acta Biomater* 2020;**111**:20-8.
20. Fan LL, Zhang BC, Xu AX, Shen ZC, Guo Y, Zhao RR, et al. Carrier-free, pure nanodrug formed by the self-assembly of an anticancer drug for cancer immune therapy. *Mol Pharmaceut* 2018;**15**:2466-78.

21. Wang YM, Wysocka J, Sayegh J, Lee YH, Perlin JR, Leonelli L, et al. Human PAD4 regulates histone arginine methylation levels *via* demethylation. *Science* 2004;**306**:279-83.
22. Koushik S, Joshi N, Nagaraju S, Mahmood S, Mudeenahally K, Padmavathy R, et al. PAD4: pathophysiology, current therapeutics and future perspective in rheumatoid arthritis. *Expert Opin Ther Targets* 2017;**21**:433-47.
23. Jones JE, Slack JL, Fang PF, Zhang XS, Subramanian V, Causey CP, et al. Synthesis and screening of a haloacetamide containing library to identify PAD4 selective inhibitors. *ACS Chem Biol* 2012;**7**:160-5.
24. Teixeira Á, Garasa S, Gato M, Alfaro C, Migueliz I, Cirella A, et al. CXCR1 and CXCR2 chemokine receptor agonists produced by tumors induce neutrophil extracellular traps that interfere with immune cytotoxicity. *Immunity* 2020;**52**:856-71.
25. Albregues J, Shields MA, Ng D, Park CG, Ambrico A, Poindexter ME, et al. Neutrophil extracellular traps produced during inflammation awaken dormant cancer cells in mice. *Science* 2018;**361**:eaao4227.
26. Jones JE, Causey CP, Knuckley B, Slack-Noyes JL, Thompson PR. Protein arginine deiminase 4 (PAD4): current understanding and future therapeutic potential. *Curr Opin Drug Discov Devel* 2009;**12**:616–27.
27. Demers M, Wong SL, Martinod K, Gallant M, Cabral JE, Wang YM, et al. Priming of neutrophils toward NETosis promotes tumor growth. *Oncoimmunology* 2016;**5**:e1134073.
28. Nie M, Yang LB, Bi XW, Wang Y, Sun P, Yang H, et al. Neutrophil extracellular traps induced by IL8 promote diffuse large B-cell lymphoma progression *via* the TLR9 signaling. *Clin Cancer Res* 2019;**25**:1867-79.
29. Swietach P. What is pH regulation, and why do cancer cells need it?. *Cancer Metastasis Rev* 2019;**38**:5-15.
30. Huang XL, Borgström B, Stegmayr J, Abassi Y, Kruszyk M, Leffler H, et al. The molecular basis for inhibition of stemlike cancer cells by salinomycin. *ACS Cent Sci* 2018;**4**:760-7.
31. Jiang HJ, Zhang L, Chen J, Liu MH. Hierarchical self-assembly of a porphyrin into chiral macroscopic flowers with superhydrophobic and enantioselective property. *ACS Nano* 2017;**11**:12453-60.
32. Nikoofard N, Maghsoodi F. Dynamic stability of nano-fibers self-assembled from short amphiphilic A6D peptides. *J Chem Physics* 2018;**148**:134903.

33. Li SK, Xing RR, Chang R, Zou QL, Yan XH. Nanodrugs based on peptide-modulated self-assembly: design, delivery and tumor therapy. *Curr Opin Colloid Interface Sci* 2018;**35**:17-25.
34. Cheng J, Feng SB, Han SL, Zhang XJ, Chen YD, Zhou X, et al. Facile assembly of cost-effective and locally applicable or injectable nanohemostats for hemorrhage control. *ACS Nano* 2016;**10**:9957-73.
35. Wang YJ, Li PX, Wang S, Hu J, Chen XA, Wu JH, et al. Anticancer peptidylarginine deiminase (PAD) inhibitors regulate the autophagy flux and the mammalian target of rapamycin complex 1 activity. *J Biol Chem* 2012;**287**:25941-53.
36. Hu X, Zhao M, Wang YJ, Wang YN, Zhao SR, Wu JH, et al. Tetrahydro-*b*-carboline-3-carboxyl-thymopentin: a nano-conjugate for releasing pharmacophores to treat tumor and complications. *J Mater Chem B* 2016;**4**:1384-97.
37. Gan TP, Wang YJ, Zhao M, Wu JH, Yang J, Peng SQ. 5-(Bis(3-(2-hydroxyethyl)-1*H*-indol-2-yl)methyl)-2-hydroxybenzoic acid (BHIMHA): showing a strategy of designing drug to block lung metastasis of tumors. *Drug Des Dev Ther* 2016;**10**:711-21.
38. Mondal S, Thompson PR. Protein arginine deiminases (PADs): biochemistry and chemical biology of protein citrullination. *Acc Chem Res* 2019;**52**:818-32.
39. Guo Y, Jiang K, Shen ZC, Zheng GR, Fan LL, Zhao RR, et al. A small molecule nanodrug by self-assembly of dual anticancer drugs and photosensitizer for synergistic near-Infrared cancer theranostic. *ACS Appl Mater Interfaces* 2017;**9**:43508-19.
40. Ho VHB, Slater NKH, Chen RJ. pH-responsive endosomolytic pseudo-peptides for drug delivery to multicellular spheroids tumour models. *Biomaterials* 2011;**32**:2953-8.
41. Augustine R, Kalva N, Kim HA, Zhang Y, Kim I. pH-Responsive polypeptide-based smart nano-carriers for theranostic applications. *Molecules* 2019;**24**:2961.
42. Koo H, Lee H, Lee S, Min KH, Kim MS, Lee DS, et al. *In vivo* tumor diagnosis and photodynamic therapy via tumoral pH-responsive polymeric micelles. *Chem Commun* 2010;**46**:5668.
43. Jeena MT, Palanikumar L, Go EM, Kim I, Kang MG, Lee S, et al. Mitochondria localization induced self-assembly of peptide amphiphiles for cellular dysfunction. *Nat Commun* 2017;**8**:26.
44. Du C, Qi YQ, Zhang YL, Wang YZ, Zhao X, Min H, et al. Epidermal growth factor receptor-targeting peptide nanoparticles simultaneously deliver gemcitabine and olaparib to treat pancreatic cancer with breast cancer 2 (BRCA2) mutation. *ACS Nano* 2018;**12**:10785-96.

45. Feng QQ, Zhao M, Gan TP, Zhu HM, Wang YN, Zhao SR, et al. DHDMIQK(KAP): a novel nano-delivery system of dihydroxyl-tetrahydro-isoquinoline-3-carboxylic acid and KPAK towards the thrombus. *J Mater Chem B* 2016;**4**:5991-6003.
46. Wang YJ, Tang JC, Zhu HM, Jiang XY, Liu JW, Xu WY, et al. Aqueous extract of *Rabdosia rubescens* leaves: forming nanoparticles, targeting P-selectin, and inhibiting thrombosis. *Int J Nanomed* 2015;**10**:6905-18.
47. Zheng B, Wang F, Dong SY, Huang FH. Supramolecular polymers constructed by crown ether-based molecular recognition. *Chem Soc Rev* 2012;**41**:1621-36.
48. Park W, Park S, Na K. The controlled photoactivity of nanoparticles derived from ionic interactions between a water soluble polymeric photosensitizer and polysaccharide quencher. *Biomaterials* 2011;**32**:8261-70.
49. Kong HT, Zhang Y, Li YJ, Cui ZF, Xia K, Sun YH, et al. Size-dependent cytotoxicity of nanocarbon blacks. *Int J Mol Sci* 2013;**14**:22529-43.
50. Sakai-Kato K, Un K, Nanjo K, Nishiyama N, Kusuhara H, Kataoka K, et al. Elucidating the molecular mechanism for the intracellular trafficking and fate of block copolymer micelles and their components. *Biomaterials* 2014;**35**:1347-58.
51. Gao N, Fang X. Synthesis and development of graphene–inorganic semiconductor nanocomposites. *Chem Rev* 2015;**115**:8294-343.
52. Luo YY, Xiong XY, Cheng F, Gong YC, Li ZL, Li YP. The targeting properties of folate-conjugated Pluronic F127/poly (lactic-co-glycolic) nanoparticles. *Int J Biol Macromol* 2017;**105**:711-9.
53. Simeon RL, Chamoun AM, McMillin T, Chen ZL. Discovery and characterization of a new cell-penetrating protein. *ACS Chem Biol* 2013;**8**:2678-87.
54. Vivot K, Benahmed MA, Seyfritz E, Bietiger W, Elbayed K, Ruhland E, et al. A metabolomic approach (¹H HRMAS NMR spectroscopy) supported by histology to study early post-transplantation responses in islet-transplanted livers. *Int J Biol Sci* 2016;**12**:1168-80.
55. Yu MF, Liu Y, Yu XW, Li JH, Zhao WQ, Hu JA, et al. Enhanced osteogenesis of quasi-three-dimensional hierarchical topography. *J Nanobiotechnology* 2019;**17**:102.
56. Ostroumov D, Fekete-Drimusz N, Saborowski M, Kühnel F, Woller N. CD4 and CD8 T lymphocyte interplay in controlling tumor growth. *Cell Mol Life Sci* 2018;**75**:689-713.
57. Wagner J, Rapsomaniki MA, Chevrier S, Anzeneder T, Langwieder C, Dykgers A, et al. A single-cell atlas of the tumor and immune ecosystem of human breast cancer. *Cell* 2019;**177**:1330-45.

58. Wculek SK, Cueto FJ, Mujal AM, Melero I, Krummel MF, Sancho D. Dendritic cells in cancer immunology and immunotherapy. *Nat Rev Immunol* 2020;**20**:7-24.
59. Vladimirovna IL, Sosunova E, Nikolaev A, Nenasheva T. Mesenchymal stem cells and myeloid derived suppressor cells: common traits in immune regulation. *J Immunol Res* 2016;**2016**:7121580.
60. Andrews LP, Marciscano AE, Drake CG, Vignali DAA. LAG3 (CD223) as a cancer immunotherapy target. *Immunol Rev* 2017;**276**:80-96.
61. Woo SR, Turnis ME, Goldberg MV, Bankoti J, Selby M, Nirschl CJ, et al. Immune inhibitory molecules LAG-3 and PD-1 synergistically regulate T-cell function to promote tumoral immune escape. *Cancer Res* 2012;**72**:917-27.
62. Bellavita R, Falanga A, Buommino E, Merlino F, Casciaro B, Cappiello F, et al. Novel temporin L antimicrobial peptides: promoting self-assembling by lipidic tags to tackle superbugs. *J Enzym Inhib Med Ch* 2020;**35**:1751-64.
63. Song SL, Gui L, Feng QQ, Taledaohan A, Li YM, Wang W et al. TAT-modified gold nanoparticles enhance the antitumor activity of PAD4 inhibitors. *Int J Nanomedicine* 2020;**15**:6659-71.
64. Verdeil G, Lawrence T, Schmitt-Verhulst A, Auphan-Anezin N. Targeting STAT3 and STAT5 in tumor-associated immune cells to improve immunotherapy. *Cancers* 2019;**11**:1832.
65. Zou SL, Tong QY, Liu BW, Huang W, Tian Y, Fu XH. Targeting STAT3 in cancer immunotherapy. *Mol Cancer* 2020;**19**:145.

Figure 1 Design, characterization, and principle of the pH-responsive self-assembly. (A) Docking and scoring interaction of target compounds with PAD4 protein. (B) Design of the pH-responsive self-assembly molecules. (C) TEM and SEM images of ZD-B at pH 7.4. Scale bar = 0.2 and 5.0 μm . (D) TEM and SEM images of ZD-B at pH 6.5. Scale bar = 200 nm and 1.0 μm . (E) TEM and SEM images of ZD-E-1 at pH 7.4. Scale bar = 50 and 500 nm. (F) TEM and SEM images of ZD-E-1 at pH 6.5. Scale bar=200 and 500 nm. (G) Size and (H) zeta potentials of ZD-B and ZD-E-1 at different pH within 6 days (assayed on Days 0, 2, 4, and 6). (I–J) Critical aggregation concentration (CAC) of ZD-E-1 at pH 7.4 and pH 6.5. (K) Drug release curve of ZD-E-1 at pH 7.4 and 6.5. Data are presented as mean \pm SD ($n = 3$).

Figure 2 Self-assembly characteristics of ZD-B and ZD-E-1. (A and B) Fourier-transform mass spectrometry of ZD-B and ZD-E-1 in pH 7.4 solution. (C and D) NOSEY 2D NMR spectrum of ZD-B and ZD-E-1. (E and F) Molecular dynamics simulation of ZD-B and ZD-E-1 and interaction of molecules in self-assembled nano-units.

Figure 3 Intracellular morphology, localization, and cytotoxicity of self-assembled molecules. (A) Intracellular morphology of 50 $\mu\text{mol/L}$ ZD-B after 48 h observed by fluorescence microscopy and localization of 20 $\mu\text{mol/L}$ ZD-B observed by confocal laser scanning microscopy (CLSM, Leica) in HL7702 cells. Scale bar = 25 μm . (B) Localization of 20 $\mu\text{mol/L}$ ZD-E-1 after 48 h observed by CLSM (Leica) in HL7702 cells. Scale bar = 25 μm . (C–D) Cellular localization of 20 $\mu\text{mol/L}$ ZD-B and ZD-E-1 after 48 h observed by CLSM (Leica) in 4T1 tumor cells. Scale bar = 25 μm . (E) The mean fluorescence intensity of drugs 48 h after administration determined by ImageJ software. (F and G) Cell viability of HL7702 and 4T1 tumor cells treated with 3.25, 6.25, 12.5, 25, 50, and 100 $\mu\text{mol/L}$ ZD-B and ZD-E-1 for 48 h. (H) IC_{50} of ZD-B and ZD-E-1 of HL7702 and 4T1 cells. (I) Representative CLSM images from different time points. Scale bar = 25 μm . (J) Curves of mean fluorescence intensity determined by ImageJ at the different time points. Data are presented as mean \pm SD ($n = 3$). $**P < 0.01$.

Figure 4 *In vitro* activity of ZD-E-1. (A) H3cit protein expression and subcellular colocalization of 10 $\mu\text{mol/L}$ ZD-E-1 and H3cit protein in 4T1 cells determined by CLSM (Leica). Scale bar = 50 μm . (B) Radial distribution of green and red fluorescence intensity analyzed by ImageJ. (C) Mean fluorescence intensity of H3cit calculated by ImageJ. (D and E) Effect of 10 $\mu\text{mol/L}$ drug on ability

of neutrophils to release NETs. Scale bar = 50 μm . (F and G) Representative images and analysis of transwell assay. a–e was control, 10 $\mu\text{mol/L}$ RGDS, 10 $\mu\text{mol/L}$ ZD-E-1, 5 $\mu\text{mol/L}$ ZD-E-1, and 2 $\mu\text{mol/L}$ ZD-E-1, respectively. Scale bar=100 μm . (H and I) Morphological changes in cells in the control and 10 $\mu\text{mol/L}$ ZD-E-1 administration groups observed by TEM (Hitachi) and SEM (Hitachi). TEM scale bar = 1 and 0.5 μm . SEM scale bar = 20 and 10 μm . Data are presented as mean \pm SD ($n = 3$). $*P < 0.05$ and $**P < 0.01$.

Figure 5 Effect of nanodrugs ZD-B and ZD-E-1 on S180 tumor-bearing mice. (A and B) Tumor volume and tumor weight. (C) Mean fluorescence of H3cit, $n = 3$ biologically independent animals. (D) Distribution and the H3cit expression of ZD-E-1 in tumor tissues at 24 h after administration. Scale bar = 200 μm . (E) Radial distribution of green and red fluorescence intensity analyzed by ImageJ. (F) Fluorescence images of S180 tumor-bearing ICR mice main organs after single dose administration. (G) Radiant efficiency of tumor at various time points. (H and I) Responsive images Image and statistical analysis of CD4 and CD8a expression in tumor tissues. Scale bar = 200 μm . Data are presented as mean \pm SD ($n = 3$). $*P < 0.05$ and $**P < 0.01$.

Figure 6 Effect of nanodrug ZD-E-1 on 4T1 orthotopic tumor-bearing mice. (A) Treatment scheme of BALB/c mice. (B and C) Tumor volume and tumor weight of 4T1 orthotopic tumor-bearing mice. (D) Tumors from mice of each group. Scale bar = 1 cm. (E) Representative images of metastasis in the lung. Scale bar = 2000 and 100 μm . (F) The number of pulmonary metastases. (G) Representative images of HE staining of lung tissue sections. (H) Representative images of NETs formation in 4T1 tumor sections. Scale bar = 100 μm . (I) Statistics of H3cit and Ly6G expression in tumor tissue. Data are presented as mean \pm SD ($n = 3$). $*P < 0.05$ and $**P < 0.01$.

Figure 7 Effect of ZD-E-1 on tumor immune microenvironment. (A) Scheme of single-cell mass cytometry experiment. (B) t-Distributed stochastic neighbor embedding (tSNE) plot showing protein expression. (C) tSNE plot for immune cells from LLC tumor. (D) DCs, MDSCs, and CD4 T cell frequency (percent of CD45⁺ cells) in tumor tissue. (E) Expression of LAG3 protein in different cell groups. (F) Expression of CXCR3 and CCR4 protein in CD4 or CD8 T cells. (G) Effect of ZD-E-1 on immune cells and functional protein in tumor tissue. Data are presented as mean \pm SD ($n = 3$). $*P < 0.05$ and $**P < 0.01$.

Figure 8 Combination immunotherapy with PAD4 inhibitor ZD-E-1 and PD1 antibody on LLC tumor-bearing C57BL/6 mice. (A) Treatment scheme of C57BL/6 mice. (B) Pictures of LLC tumors from C57BL/6 mice of each group. Scale bar = 1 cm. (C and D) Tumor volume and tumor weight of LLC tumor-bearing C57BL/6 mice. (E) Representative images of metastasis in the lung. (F) The number of pulmonary metastases. (G) Representative images of HE staining of lung tissue sections. Scale bar = 2000 and 100 μm . (H) Survival curve of C57BL/6 mice bearing LLC tumor. (I) Immunofluorescence staining for LAG3 (red) of tumor sections. Scale bar = 100 μm . (J) Statistical analysis of LAG3 expression measured with ImageJ. (K and L) Expression of IFN- γ and TNF- α in tumor tissue and serum determined by ELISA kit. Data are presented as mean \pm SD ($n = 3$). * $P < 0.05$ and ** $P < 0.01$.

Figure 9 Self-assembly and action mechanism of ZD-E-1.

